Journal of Solid State Chemistry 184 (2011) 199–203

Contents lists available at ScienceDirect

Journal of Solid State Chemistry

journal homepage: www.elsevier.com/locate/jssc

Intrinsic magnetism in Fe doped SnO_2 nanoparticles

S. Sambasivam [a,b], Byung Chun Choi [b], J.G. Lin [a,*]

[a] Center for Condensed Matter Sciences, National Taiwan University, Taipei 10617, Taiwan
[b] Department of Physics, Pukyong National University, Busan 608-737, Republic of Korea

ARTICLE INFO

Article history:
Received 26 August 2010
Received in revised form
21 October 2010
Accepted 7 November 2010
Available online 18 November 2010

Keywords:
DMS
Nanoparticles
ESR
Magnetic study

ABSTRACT

Iron doped semiconducting nanoparticles $Sn_{1-x}Fe_xO_2$ with $x=0$, 0.001, 0.002, 0.003, 0.004, 0.01 and 0.03 were prepared by a sol–gel method. The X-ray diffraction, Transmission Electron Microscopy measurements confirm the rutile structure with no impurity phase. The three characteristic lines of electron spin resonance (ESR) are observed in the doped samples for all compositions, which is a clear evidence for rhombic Fe^{3+} in rutile phase. The line width of ESR increases with increase in Fe concentration due to induced disorder. The spin-pumping effect is observed at temperatures below 250 K for the samples with $x=0.01$ and 0.03. However, based on the Curie–Weiss susceptibility, iron is in paramagnetic state and is subject to weak antiferromagnetic interaction. Blue shift in the optical band gap is observed with increase in the Fe content.

1. Introduction

During the last few years, there has been extensive interest in the diluted magnetic semiconductors (DMSs) for their potential applications in spintronic devices that allow the control of both the spin and charge carriers [1,2]. Although there is an interesting physics behind the mechanism of ferromagnetism in DMSs [3–7], the low saturation moment and the low Curie temperature (T_C) make them hardly usable in practical devices. The first dilute magnetic semiconducting property was observed in intrinsically *p*-type Mn-doped GaAs around 110 K [8]. Theoretical calculations predicted room-temperature ferromagnetism with exchange interaction mediated by *p*-type free carriers in transition-metal doped ZnO and GaN semiconductors [9]. Recently various experiments have carried out on ZnO [10–13], ZnS [14], SnO_2 [4,15,16], TiO_2 [17] and Cr doped $CuZnSe_2$ [18] DMS, regarding the presence or absence of ferromagnetism. Adhikari et al. [19] reported the synthesis of Fe doped tin dioxide (SnO_2) nanoparticles by a chemical coprecipitation method and found that the antiferromagnetic interaction reduces with the increasing Fe content. Lee et al. [20] reported that the ferromagnetic characteristics were enhanced by increasing the Fe content in TiO_2 samples.

Among various semiconductors, SnO_2 has a wide band gap ($E_g=3.6$ eV at 300 K) with *n*-type carriers [21,22], which makes it a potential system to become room temperature DMS by doping with magnetic ions. However, the controversy between the intrinsic or extrinsic ferromagnetism must be clarified before one can really design the related devices. Coey et al. [4] reported a high Curie temperature of 610 K in a $Sn_{0.95}Fe_{0.05}O_2$ thin film. In this work, we prepare a series of Fe-doped SnO_2 nanoparticles for studying the detailed magnetic behavior of this system via the electron spin resonance (ESR) measurements. ESR is a powerful tool to study the local spin-structure of iron ions. Important information can be obtained concerning the interplay of different interactions through a study on various ESR parameters such as resonance field H_r, *g*-value, peak-to-peak line width and resonance intensity. In particular, the local symmetry of Fe-ion can be explored by monitoring its fine-structure via the modification of oxygen vacancies [23]. It was shown that if charge compensation occurs in the nearest-neighbor O^{2-} ion shell, a large distortion in the octahedral symmetry occurs, and a significant change of the intrinsic Fe^{3+} fine-structure tensor could be induced.

2. Experimental details

Fe doped SnO_2 nanoparticles for the nominal composition of $Sn_{1-x}Fe_xO_2$ are $x=0.0$, 0.001, 0.002, 0.003, 0.004, 0.01 and 0.03 were prepared by the sol–gel method. After 3.5 g of tin chloride (hydrous $SnCl_4\cdot 5H_2O$) dissolved in 75 mL of distilled water at 80 °C, citric acid was added to reach pH=1.5. Appropriate amount of ferric chloride ($FeCl_3\cdot 6H_2O$) was dissolved in distilled water along with 6 mL of poly glycol with continuous stirring for 10 min. Ammonia solution ($NH_3\cdot H_2O$—28%) was then added dropwise until pH=8. The hydrolysis product is stirred for 3 h to form a gel. Finally, the samples were dried at 120 °C for 12 h and calcined at 400 °C in air for 2 h. The X-ray diffraction (XRD) patterns were obtained using Bruker 8. Transmission Electron Micrographs (TEM)

* Corresponding author. Fax: +886 02 33665219.
E-mail address: jglin@ntu.edu.tw (J.G. Lin).

0022-4596/$ - see front matter © 2010 Elsevier Inc. All rights reserved.
doi:10.1016/j.jssc.2010.11.010

were recorded in (JEOL-TEM 2010) with an accelerating voltage of 200 kV. The electron spin resonance (ESR) spectra of powder samples of all compositions were recorded at various temperatures (T) from 300 to 80 K using an X-band Bruker ER-041 spectrometer. The magnetic measurements were carried out using a superconducting quantum interference device (SQUID, Quantum Design MPMS-XL7). The optical absorption measurements were performed in a JASCO-V-670 spectrophotometer.

3. Results and discussion

Fig. 1 shows the powder X-ray diffraction (XRD) patterns of pure and Fe doped SnO_2 samples. All peaks are indexed based on the tetragonal lattice of SnO_2 (rutile structure). The diffraction data are in good agreement with JCPDS file no. 21-1250.The diffraction planes are broadened, and the intensity decreases by increasing the Fe content due to the decrease in crystallite size by increasing the Fe content. The peak position also shifts towards lower angle indicating the expansion of lattice (see Table 1). In general, when an element of smaller ionic radii (Fe^{3+}, 0.64 Å) is substituted for a large size ionic site (Sn^{4+}, 0.71 Å), the lattice constants decrease. In the case of Fe doped SnO_2 Adhikari et al. report [19] that the lattice parameters do not indicate a definitive trend in variation. In our samples, we do observe the increase in 'c' lattice constant as well as the cell volume by increasing the Fe content. Since the valence of Fe^{3+} is different from Sn^{4+}, we speculate that the oxygen defect may be the another factor to influence the size of unit cell. No impurity peaks are observed in all measured samples. The absence of secondary phase may be attributed to the superiority of the sol–gel method in yielding a sample with dopants distributed homogenously without clustering or segregation [24]. The lattice parameters and average crystallite size of samples determined from the Scherrer equation are given in Table 1. The TEM image of $Sn_{1-x}Fe_xO_2$ ($x=0.01$) is shown in Fig. 2. The crystallite size of the sample with $x=0.01$ is found to be isolated and nearly spherical in shape. The selected area electron diffraction (SAED) pattern is also shown in the inset of Fig. 2. From the SAED rings, it is identified to have a rutile structure with diffraction planes corresponding to (110), (101), (200), (211), (220), (002) and (310). No impurity phase could be identified. The distribution plot fitted with a Gaussian profile is shown in Fig. 3. The average crystallite size obtained is

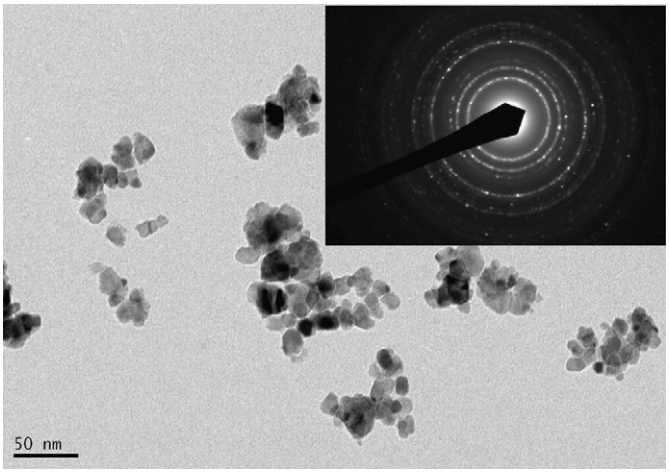

Fig. 2. TEM micrograph of $Sn_{1-x}Fe_xO_2$ ($x=0.01$) nanoparticles with the inset showing the corresponding SAED pattern.

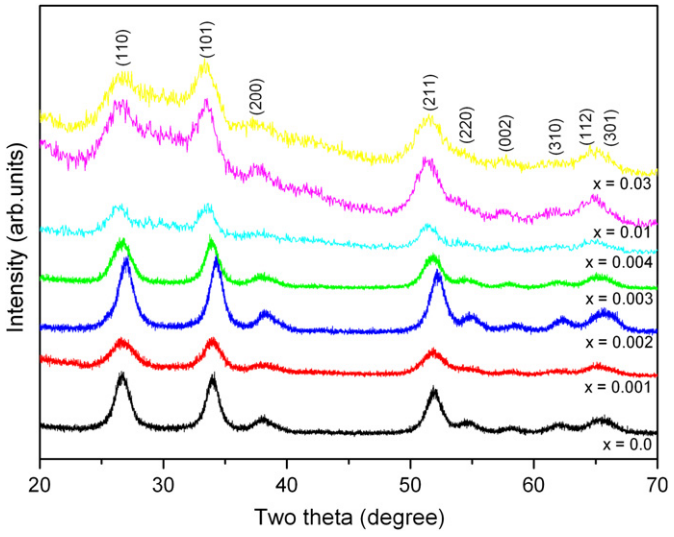

Fig. 1. XRD patterns of $Sn_{1-x}Fe_xO_2$ ($x=0.0$, 0.001, 0.002, 0.003, 0.004, 0.01 and 0.03) nanoparticles.

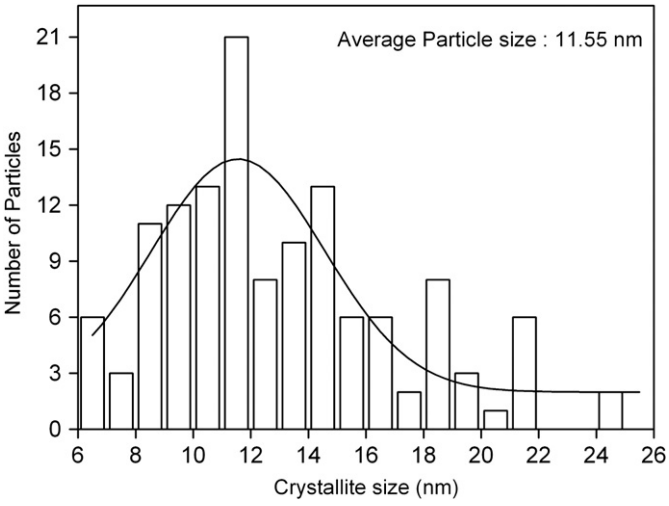

Fig. 3. Size distribution plot from the TEM micrograph of $Sn_{1-x}Fe_xO_2$ ($x=0.01$) nanoparticles.

Table 1
Lattice parameters, cell volume, average crystallite size and band gap values of $Sn_{1-x}Fe_xO_2$ ($x=0$, 0.001, 0.002, 0.003, 0.004, 0.01 and 0.03) samples.

Sample ID	$a=b$ (Å)	c (Å)	Cell volume (Å^3)	Crystallite size (nm)	Band gap (eV)
Pure SnO_2	4.724	3.175	70.856	18.75	4.06
0.001 Fe in SnO_2	4.723	3.178	70.902	17.25	4.18
0.002 Fe in SnO_2	4.749	3.177	71.677	16.0	4.21
0.003 Fe in SnO_2	4.762	3.189	72.315	15.37	4.35
0.004 Fe in SnO_2	4.772	3.215	73.236	14.73	4.39
0.01 Fe in SnO_2	4.764	3.226	73.217	12.8	4.44
0.03 Fe in SnO_2	4.762	3.226	73.157	11.10	4.47

11.5 nm; this is in good agreement with the size obtained from XRD results (Table 1).

The ESR spectra were taken for all the samples. No ESR signal was detected in the undoped SnO_2. Fig. 4 is the plot of derivative of ESR spectra at 80 K for all doped samples and Fig. 5 is the temperature dependent ESR spectrum for $x=0.004$. In both the figures, three lines are observed, which are denoted as g_1, g_2 and g_3 with the dashed lines marking the positions of resonance field H_r. The effective g-factor is determined according to the equation $g=h\nu/\mu_B H_r$, where h is Planck's constant, ν is the microwave frequency and μ_B is the Bohr magneton. The g-values of three lines are $g_1 \cong 4.2 \pm 0.1$, $g_2 \cong 5.6 \pm 0.1$ and $g_3 \cong 8.1 \pm 0.1$, which are the typical values corresponding to the isolated rhombic Fe^{3+} ions in rutile structure [25]. These resonance spin states occur as a consequence of strong crystal fields and are related to the spin–orbit coupling constant, the orbital reduction factor and the energy-level splitting of the $(t_{2g})^5$ states of the Fe^{3+} ion [26,27]. Fig. 6 shows the values of three g-values vs. T, indicating clearly that they are nearly a constant at all temperatures. ΔH is defined as the peak to peak line width, and the typical ΔH for the strongest peak increases by decreasing T and increasing x as shown in Fig. 7. The

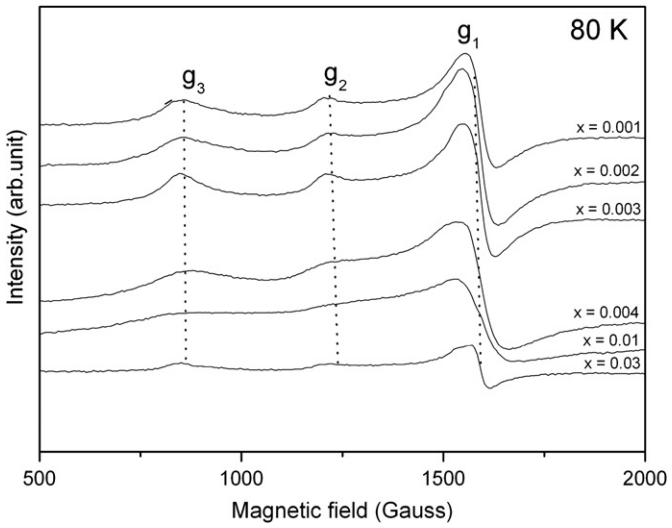

Fig. 4. ESR spectra of $Sn_{1-x}Fe_xO_2$ ($x=0.001$, 0.002, 0.003, 0.004, 0.01 and 0.03) at 80 K.

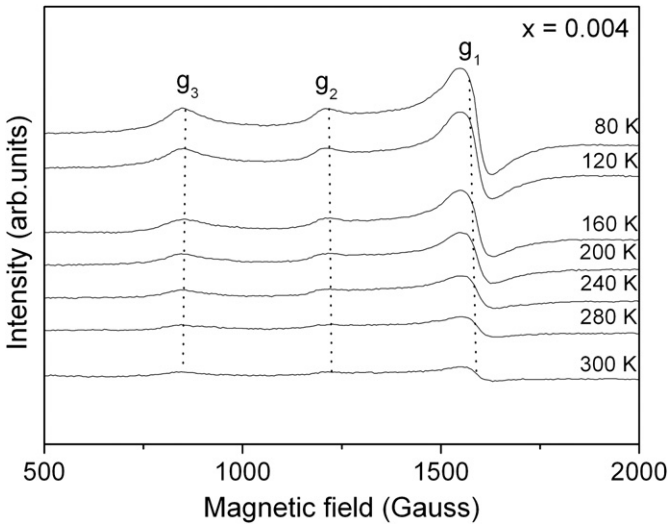

Fig. 5. Temperature dependence of the ESR spectra of $Sn_{1-x}Fe_xO_2$ ($x=0.004$).

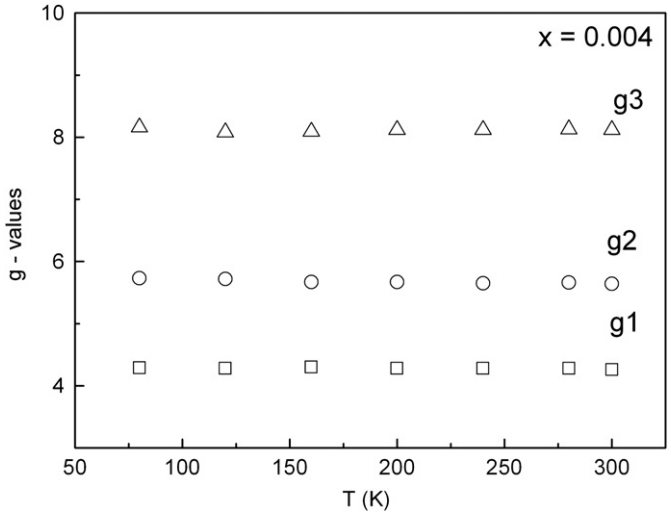

Fig. 6. g-Values at different temperatures of $Sn_{1-x}Fe_xO_2$ ($x=0.004$) extracted from the ESR spectra.

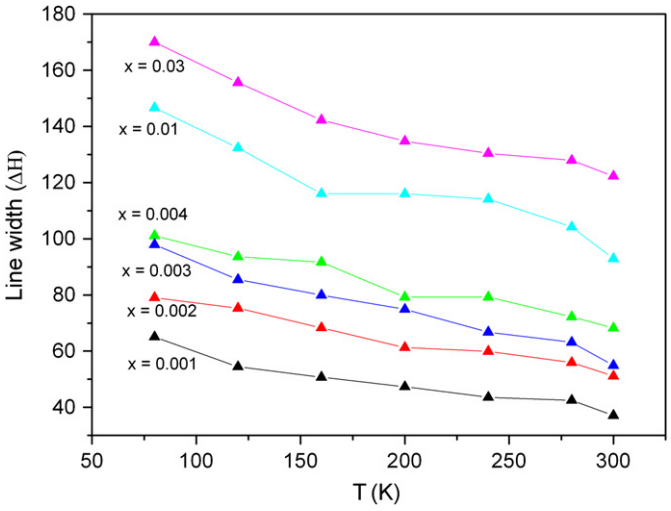

Fig. 7. Temperature dependence of ESR line width of $Sn_{1-x}Fe_xO_2$ nanoparticles.

increase in ΔH by decreasing T is related to the thermal effect on the spin relaxation time and by increasing x is due to the enhancement of ionic disorder. The number of spins in a unit volume is proportional to the area under the major ESR line and can be determined by its double integral. The T-dependent area for all doped samples is shown in Fig. 8 indicating an up-shift of curve with increase in x. However, the rate of increase with decreasing temperature for all doped samples is nearly the same except for the samples with high x. For $x=0.01$ and 0.03, the spin number starts to increase sharply below $T=250$ K, implying an extra spin-pumping.

The field cooled (FC) and zero field cooled (ZFC) magnetization M as a function of T for $Sn_{1-x}Fe_xO_2$ with $x=0.01$ and 0.03 are shown in Figs. 9(a) and (b), respectively. The FC- and ZFC-$M(T)$ curves almost coincide in both figures, showing a typical paramagnetic behavior. For a quantitative assessment of the intrinsic exchange coupling between Fe ions, Curie–Weiss plots are made from the inverse molar susceptibility $(1/\chi)$ vs. T based on the FC-$M(T)$ curves in a magnetic field of 500 Oe for $Sn_{0.99}Fe_{0.01}O_2$ and $Sn_{0.97}Fe_{0.03}O_2$, as shown in the inset of Figs. 9(a) and (b). The inverse susceptibility can be well fitted using the Curie–Weiss law

$$\frac{1}{\chi} = \frac{T-\theta}{C} \quad (1)$$

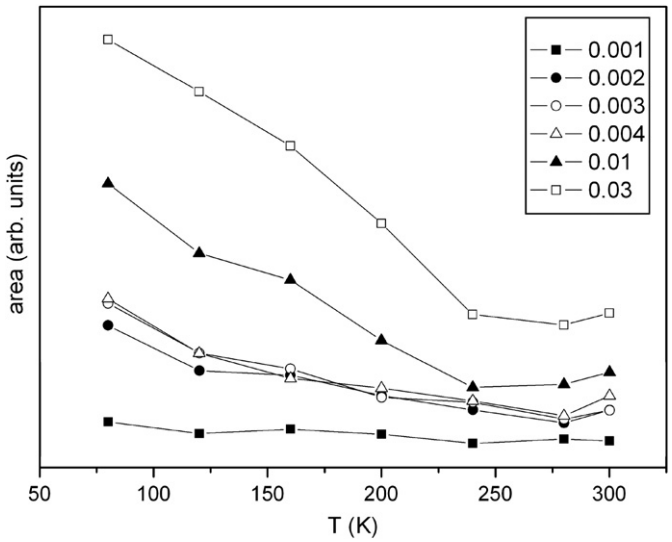

Fig. 8. Temperature dependence of relative number of spins (Ns) of $Sn_{1-x}Fe_xO_2$ nanoparticles from the ESR spectra.

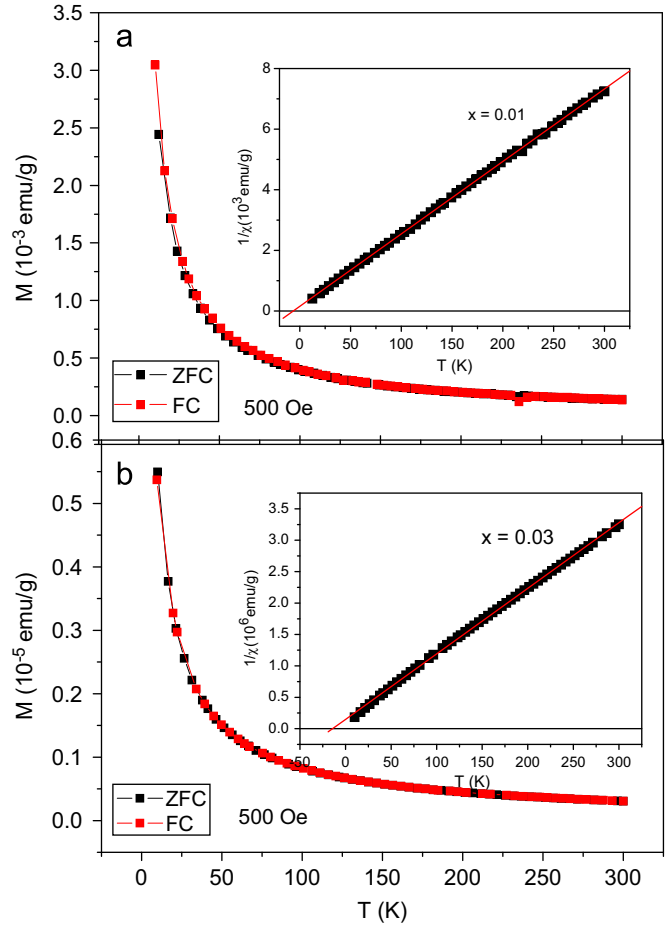

Fig. 9. $M(T)$ curves of $Sn_{1-x}Fe_xO_2$ nanoparticles with $x=0.01$ (a) and $x=0.03$ (b). The respective inset shows the variation of the inverse susceptibility with temperature.

where C is the Curie constant and θ is the Curie–Weiss temperature. Value of θ is -6.78 and -14.33 for samples with $x=0.01$ and 0.03, respectively, indicating the existence of antiferromagnetic interactions in the ground state. In conjunction with the ESR data, it is reasonable to suggest that the isolated Fe^{3+} ions in $Sn_{1-x}Fe_xO_2$ are paramagnetic but experience weak antiferromagnetic interaction. Compared to the previous ESR study in Co-doped ZnS [14], it is our speculation that the absence of ferromagnetism in $Sn_{1-x}Fe_xO_2$ may be because of the lack of free carriers.

The UV–visible absorption spectra of SnO_2 and Fe doped SnO_2 samples are shown in Fig. 10. Broad and asymmetrical peaks occur at about 200–350 nm, which is distinct from the case of the bulk sample. The broad peak is attributed to the electron–hole pairs caused by the quantum confinement, i.e. an exciton energy level. The optical band gap is determined from the peak position. The asymmetrical shape of the exciton absorption peaks cannot be explicitly explained at the present stage but might be attributed to the collisions between excitons by thermal vibration. A small shift towards the lower wavelength region in the absorption edge of tin oxide is observed with increasing Fe content. Based on the XRD, the crystallite size of the samples decreases from 18.75 to 11 nm by increasing the Fe content (see Table 1). It is clear from the band gap estimated from the absorption spectra of nanoparticles to show a blue shift by increasing the Fe content (inset of Fig. 10). According to Kayanuma's theory [28] on the quantum confinement of an electron–hole pair in a spherical well, the band-gap energy E_g is determined by the characteristic distance (or radius, R) in the following equation:

$$E_g(R) = E_g^0 + \frac{\hbar^2\pi^2}{2\mu R^2} - \frac{1.786e^2}{\varepsilon R} - \frac{0.124e^4\mu}{\hbar^2\varepsilon^2} \quad (2)$$

where ε is the dielectric constant, R is the particle radius, is the Plank constant and $\mu = (1/m_e^* + 1/m_h^*)^{-1}$ (m_e^* and m_h^* are the effective masses of electron and hole, respectively). The second term is the quantum confinement energy for electron and hole in a spherical particle, which is larger than the Coulomb attraction energy and the exchange energy (the third and fourth term) as R decreases. As shown from the equation, the band-gap energy E_g increases with decrease in particle size. The estimated band-gap energy E_g and crystallite size R for various Fe contents are shown using Eq. (2). It is clearly demonstrated that the nanometer-sized particles exhibit quantum size effect with blue shift (absorption edge was found to shift to shorter wavelength) of band-gap energy with an increase in the Fe content as shown in the inset of Fig. 10 and Table 1. Similar size effect has been reported in case of doped SnO_2 and TiO_2 nanoparticles with shift towards lower wavelength region in their absorption spectra [29,30].

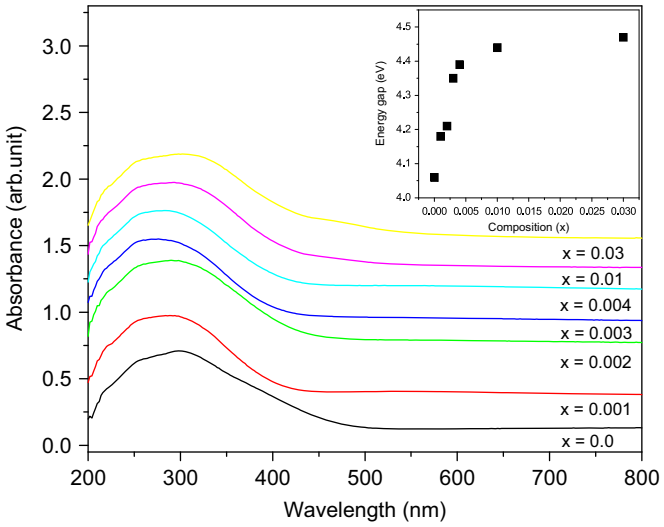

Fig. 10. Optical absorption spectra of $Sn_{1-x}Fe_xO_2$ ($x=0.0$, 0.001, 0.002, 0.003, 0.004, 0.01 and 0.03) nanoparticles. Inset shows the blue shift in the band gap of SnO_2 nanoparticles as a function of Fe concentration.

4. Conclusions

In this work, a series of Fe doped SnO_2 nanoparticles was prepared by the sol–gel method. Structure of the samples is found to be rutile and the crystallite size is found to decrease with Fe content. The *g*-values of the ESR spectra reveal that the nature of Fe in $Sn_{1-x}Fe_xO_2$ samples is isolated rhombic Fe^{3+} ion in rutile phase, and the line width of ESR increases with increase in Fe^{3+}-content due to the ion induced disorder effect. The temperature dependent magnetization confirms that the Fe^{3+}-ions have weak antiferromagnetic interactions. However, for the samples with high Fe content ($x=0.01$ and 0.03), an extra spin-pumping is observed below 250 K. The optical absorption spectra of Fe doped SnO_2 nanoparticles showed a blue shift in the band gap compared to the undoped SnO_2 sample.

Acknowledgments

The authors acknowledge the financial support from National Science Council of ROC. under Grant no. 96-2112-M-002-027-MY3 and National Taiwan University under the top-project.

References

[1] S.A. Wolf, D.D. Awschalom, R.A. Buhrman, J.M. Daughton, S. Von Molnar, M.L. Roukes, A.Y. Chtchelkanova, D.M. Treger, Science 294 (2001) 1488.
[2] G.A. Prinz, Science 282 (1998) 1660.
[3] S.B. Ogale, R.J. Choudhary, J.P. Buban, S.E. Lofland, S.R. Shinde, S.N. Kale, V.N. Kulkarni, J. Higgins, C. Lanci, J.R. Simpson, N.D. Browing, S. Das Sharma, H.D. Drew, R.L. Greene, T. Venkatesan, Phys. Rev. Lett. 91 (2003) 077205.
[4] J.M.D. Coey, A.P. Douvalis, C.B. Fitzgerald, M. Venkatesan, Appl. Phys. Lett. 84 (2004) 1332;
C.B. Fitzgerald, M. Venkatesan, A.P. Douvalis, S. Huber, J.M.D. Coey, T. Bakas, J. Appl. Phys. 95 (2004) 7390.
[5] S.K. Misra, S.I. Andronenko, K.K. Reddy, J. Hays, A. Thurber, A. Punnoose, J. Appl. Phys. 101 (2007) 09H120.
[6] J. Phillip, N. Theodoropoulou, G. Berera, J.S. Moodera, B. Satpati, Appl. Phys. Lett. 85 (2004) 777.
[7] A. Punnoose, J. Hays, V. Gopal, V. Shutthanandan, Appl. Phys. Lett. 85 (2004) 1559.
[8] F. Matsukura, H. Ohno, A. Shen, Y. Sugawara, Phys. Rev. B 57 (1998) R2037.
[9] T. Dietl, H. Ohno, F. Matsukura, J. Cibert, D. Ferrand, Science 287 (2000) 1019.
[10] A.S. Risbud, N.A. Spaldin, Z.Q. Chen, S. Stemmer, R. Seshadri, Phys. Rev. B 68 (2003) 205202.
[11] D. Paul Joseph, S. Naveenkumar, N. Sivakumar, C. Venkateswaran, Mater. Chem. Phys. 97 (2006) 188.
[12] K.C. Barick, M. Aslam, Vinayak P. Dravid, D. Bahadur, J. Phys. Chem. C 112 (2008) 15163.
[13] S. Ye, V. Ney, T. Kammermeier, K. Ollefs, A. Ney, F. Wilhelm, A. Rogalev, J. Supercond. Nov. Magn. 23 (2010) 91.
[14] S. Sambasivam, D. Paul Joseph, J.G. Lin, C. Venkateswaran, J. Solid State Chem. 182 (2009) 2598.
[15] Huaxin Zhang, Li Zhang, Huaping Zuo, Shihui Ge, J. Nanosci. Nanotechnol. 10 (2010) 5116.
[16] Li Zhang, Shihui Ge, Huaxin Zhang, Yalu Zuo, J. Nanosci. Nanotechnol. 10 (2010) 4936.
[17] Y. Matsumoto, M. Murakami, T. Shono, T. Hasegawa, Science 291 (2001) 854.
[18] D. Paul Joseph, C. Venkateswaran, Phys. Status Solidi A (2010) 1–4. doi: 10.1002/pssa.201026179.
[19] R. Adhikari, A.K. Das, D. Karmakar, T.V. Chandrasekhar Rao, J. Ghatak, Phys. Rev. B 78 (2008) 024404.
[20] H.M. Lee, S.J. Kim, I.B. Shim, C.S. Kim, IEEE Trans. Magn. 39 (2003) 2788.
[21] A.V. Tadeev, G. Delabouglise, M. Labeau, Mater. Sci. Eng. B 57 (1998) 76.
[22] D. Paul Joseph, P. Renugambal, M. Saravanan, S. Philip Raja, C. Venkateswaran, Thin Solid Films 517 (2009) 6129.
[23] G. Pecchi, P. Reyes, T. Lopez, R. Gomez, A. Moreno, J.L.G. Fierro, J. Martinez-Arias, J. Sol–Gel Sci. Technol. 27 (2003) 205.
[24] K. Nomura, C.A. Barrero, J. Sakuma, M. Takeda,, Phys. Rev. B. 75 (2007) 184411.
[25] C. Cannas, D. Gatteschi, A. Musinu, G. Piccaluga, C. Sangregorio, J. Phys. Chem. B 102 (1998) 7721.
[26] C. Daul, A. Goursot, Inorg. Chem. 24 (1985) 3554.
[27] A. Abragam, B. Bleaney, Electron Paramagnetic Resonance of Transition Ions, Oxford University Press, 1970, pp. 481–484.
[28] Y. Kayanuma, Phys. Rev. B 38 (1988) 9797.
[29] B.L. Yu, C.S. Zhu, F.X. Gan, Opt. Mater. 7 (1997) 15.
[30] W. Choi, A. Termin, M.R. Hoffmann, J. Phys. Chem. 98 (1994) 3669.